

PAPER • OPEN ACCESS

Metal nanoparticle arrays via a water-based lift-off scheme using a block copolymer template

To cite this article: Björn Landeke-Wilsmark and Carl Hägglund 2022 *Nanotechnology* **33** 325302

View the [article online](#) for updates and enhancements.

You may also like

- [In Situ Monitoring and Real-Time Control of Gate Hardmask Etching in High-Volume Manufacturing of ICs](#)
Lele Chen, Weinan Jiang, Todd Pao et al.
- [UV Laser Annealing Effect on Mechanical Properties of Boron Doped Amorphous Carbon Films As Hardmasks](#)
Chulmin Youn, Jaeyoung Yang, Sungwoo Lee et al.
- [Directed self-assembly of block copolymers for use in bit patterned media fabrication](#)
Rhys Alun Griffiths, Aled Williams, Chloe Oakland et al.



IOP | ebooks™

Bringing together innovative digital publishing with leading authors from the global scientific community.

Start exploring the collection—download the first chapter of every title for free.

Metal nanoparticle arrays via a water-based lift-off scheme using a block copolymer template

Björn Landeke-Wilmsmark and Carl Hägglund 

Division of Solar Cell Technology, Department of Materials Science and Engineering, Uppsala University, PO Box 35, SE-75103 Uppsala, Sweden

E-mail: carl.haggglund@angstrom.uu.se

Received 18 February 2022, revised 31 March 2022

Accepted for publication 5 April 2022

Published 17 May 2022



Abstract

Metal *nanoparticles* (NPs) can exhibit unique electronic, magnetic, optical, and catalytic properties. Highly ordered, dense arrays of non-close-packed, surface-supported metal NPs are thus of potential use in a wide range of applications. Implementing such arrays over large surfaces can, however, be both technologically challenging and prohibitively expensive using conventional top-down nanofabrication techniques. Moreover, many existing patterning methods are too harsh for sensitive substrate surfaces and their applications. To address this, we here investigate a fabrication protocol involving a water-based lift-off scheme in which the template pattern generation is rapidly and inexpensively achieved through *block copolymer* (BCP) self-assembly. A three-layer lift-off stack consisting of, from top to bottom, a poly(styrene-*block*-2-vinyl pyridine) template, a SiO_x intermediate hardmask, and a water-soluble poly(vinyl alcohol) sacrificial layer is employed in this endeavor. *Solvent-induced surface reconstruction* (SISR) is used to generate an initial surface topography in the BCP template which is subsequently transferred to the layers beneath in a sequence of reactive ion etching steps. Through judicious selection of stack materials and dry etch chemistries, a layered, high-aspect-ratio, nanoporous mask is thus implemented. After metal deposition, the mask and excess material are simply removed in a lift-off step by dissolving the bottommost sacrificial layer in water. The incorporation of an intermediate hardmask and a water-soluble sacrificial layer obviates the need for harmful and/or corrosive lift-off solvents and decouples the BCP self-assembly process from the influence of substrate properties. We demonstrate the generation of well-ordered arrays of Au NPs capable of supporting sharp, localized surface plasmon resonances. We also investigate improvements to large-scale uniformity, as this is found sensitive to the SISR termination step in the original protocol. Extensions of the technique to other BCP morphologies and materials deposited ought to be straightforward.

Supplementary material for this article is available [online](#)

Keywords: lift-off, water-soluble sacrificial layer, nanoparticle arrays, noble metal nanoparticles, nanoporous template, self-assembly, block copolymer lithography

(Some figures may appear in colour only in the online journal)



Original content from this work may be used under the terms of the [Creative Commons Attribution 4.0 licence](#). Any further distribution of this work must maintain attribution to the author(s) and the title of the work, journal citation and DOI.

Abbreviations

BCP	block copolymer
BP	(chamber) base pressure

c-c	center-to-center
DI	deionized
Dx	dextran
EDS	energy-dispersive x-ray spectroscopy
EF	etch factor
ER	etch rate
hPS	homopolystyrene
HSQ	hydrogen silsesquioxane
LSPR	localized surface plasmon resonance
MCE	minimum cross-entropy (algorithm)
NP	nanoparticle
PS- <i>b</i> -PxVP	poly(styrene- <i>block</i> - <i>x</i> -vinyl pyridine) ($x = 2, 4$)
PS- <i>b</i> -PMMA	poly(styrene- <i>block</i> -methyl methacrylate)
RIE	reactive ion etching
RT	room temperature ($\sim 21^\circ\text{C}$)
sccm	standard cubic centimeter per minute
SE	spectroscopic ellipsometry
SEM	scanning electron microscopy
SISR	solvent-induced surface reconstruction
STEM	scanning transmission electron spectroscopy
SVA	solvent vapor annealing

1. Introduction

As nanostructured surfaces and interfaces are of growing importance within a broad range of scientific and technological applications, identifying scalable and inexpensive methods to implement these is a critical challenge. Fabrication of large-area arrays of well-ordered, non-close-packed, surface-supported metal NPs, in particular, has garnered extensive interest due to their use within diverse fields such as plasmon-enhanced, thin-film solar cells [1–4], surface-enhanced Raman spectroscopy [5], and heterogeneous catalysis [6, 7]. Thin films of BCPs capable of spontaneously adopting periodic morphologies containing discrete nanodomains, can be utilized to this end. As pattern generation is in this case achieved through molecular self-assembly, BCP templates containing densely packed nanometer-sized features can be implemented in a rapid, scalable, and inexpensive way. A prerequisite is, however, that the constituent polymer blocks differ sufficiently in one or more properties permitting differentiation and targeted nanolithographic processing. Several strategies have been demonstrated for using BCPs in conjunction with more conventional nanofabrication techniques to generate arrays of metal NPs. For example, one strategy employs selective loading of the PxVP ($x = 2, 4$) domains in a poly(styrene-*block*-*x*-vinyl pyridine) (PS-*b*-PxVP) film with AuCl_4^- . A subsequent ashing of the sample will then simultaneously reduce Au(III) to Au(0) and remove the polymer scaffold; the end result is an array of small (diameter ≤ 10 nm) Au NPs occupying the positions of the

previous PxVP domains on the substrate surface [8, 9]. From there, electroless deposition can be used to grow the NPs to the desired size [10, 11] and shape [12–15] or to create multi-metal core-shell structures [16, 17]. A second strategy involves the use of organic-inorganic hybrid BCPs, e.g. poly(styrene-*block*-ferrocenyldimethylsilane), exhibiting high block-differential dry etching characteristics to pattern a stack underneath containing metal layers [18, 19]. In a third and fourth strategy, BCPs allowing for the selective removal of one type of block, after self-assembly, are used to create nanoporous templates through which metal is deposited onto the substrate. Either a ‘wet’ [20–23] or a ‘dry’ [23, 24] lift-off scheme is finally applied to remove the excess material. Templated electrodeposition of metal onto a conductive substrate is a fifth strategy that finds yet another use for a nanoporous polymer structure and which obviates the need for removal of excess material [25].

All of the options mentioned above have unique strengths but also specific weaknesses that can limit their applicability, especially in the context of the mentioned applications where the substrates are often sensitive and surface properties are of critical importance. The main issues with the precursor loading approach are the limited size of the resultant particles and that a prolonged or intense plasma exposure of the sample is needed to reduce the precursor, remove the BCP scaffold, and create coherent NPs [26]. In the ‘dry’ lift-off and hybrid BCP approaches, material redeposition and sputter-induced damage to the substrate can be of concern. In a ‘wet’ lift-off, creating a template conducive to the release of the top metal layer and the potential need for large amounts of hazardous or environmentally questionable solvents or corrosive etchants can be issues. For example, most instances of poly(styrene-*block*-methyl methacrylate) (PS-*b*-PMMA)-based lift-off procedures demonstrated thus far require harsh methods, such as heated piranha solution [20, 27, 28] or extended ultrasonic baths in organic solvents [21, 22, 29–32], to remove the cross-linked PS template and excess material. As for templated electrodeposition, it requires a conductive substrate and care must be taken to ensure uniform nucleation and deposition over the sample surface while simultaneously preventing non-desired deposition, for instance on the backside.

In the present work, a ‘wet’ lift-off scheme utilizing a water-soluble sacrificial layer and an intermediate hardmask in addition to the BCP template is investigated. The advantages of such a three-layer stack can be many-fold as it offers: (i) a lift-off step using a benign and inexpensive solvent, (ii) a decoupling of the BCP self-assembly from the substrate surface properties, (iii) an opportunity to tailor the ultimate nanopore aspect ratio (ratio between nanopore height and diameter at the top surface) and sidewall profile in the mask while using a thin invariant BCP layer, and (iv) a certain degree of surface planarization for the BCP film. A number of considerations must, however, be taken into account when selecting the combination of materials used in the lift-off stack. First, a set of solubility constraints as (a) the preceding layer(s) must not be deleteriously affected by the application of the subsequent one(s), (b) only marginal swelling of the

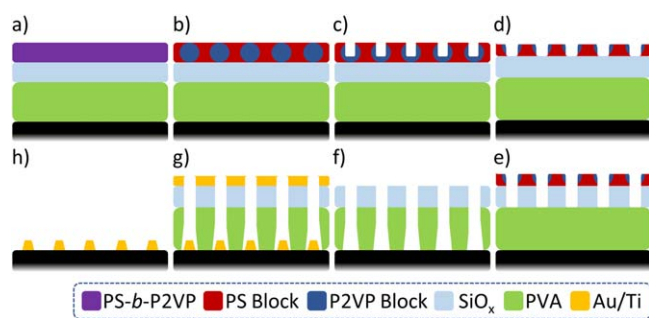


Figure 1. Schematic illustration of a lift-off procedure for generating arrays of surface-supported metal NPs using a PS-*b*-P2VP template. The individual panels represent the lift-off stack after (a) application of the sacrificial layer (PVA), the intermediate hardmask (SiO_x) and the BCP mixture (PS-*b*-P2VP + *h*PS), (b) BCP self-assembly (monolayer of P2VP spheres in a PS matrix), (c) solvent-induced surface reconstruction, (d) pore opening (RIE I, i.e. ‘descumming’), (e) SiO_x RIE (RIE II), (f) PVA RIE (RIE III), (g) metal deposition, and (h) lift-off of the layered template and excess metal by dissolving the sacrificial layer in water.

sacrificial layer (and intermediate hardmask) is desirable during the *solvent vapor annealing* (SVA) [33] and SISR [34, 35] of the BCP, and (c) the sacrificial layer must have good film-forming properties and be readily soluble in water. Second, affiliated dry etching processes with sufficiently high *etch rate* (ER) selectivity, anisotropy, and reproducibility must be available in order to faithfully transfer the BCP pattern into the underlying layers.

Linder *et al* [36] have previously evaluated various polymers for use in water-soluble sacrificial layers based on solubility and film surface roughness after spin-coating and identified a number of potential candidates, foremost of which were poly(acrylic acid) and *dextran* (Dx). For our purposes, a highly hydrolyzed, low molecular weight *poly(vinyl alcohol)* (PVA) species is also a compelling option as it exhibits negligible solubility in several relevant organic solvents yet dissolves in water [37–39]. Further, PVA is non-toxic, inexpensive, and commercially available. As a purely organic polymer, PVA can moreover be etched with extremely high selectivity toward oxide hardmasks in an oxygen plasma.

As for the intermediate hardmask, SiO_x has multiple advantages such as being a well-known entity in micro-/nanofabrication with regards to both deposition and etching. Low-temperature deposition methods include atomic layer deposition [40], chemical vapor deposition [41], (reactive) sputter deposition, e-beam evaporation, and spin-coating from a *spin-on-glass* formulation e.g. a *hydrogen silsesquioxane* (HSQ) resist. To achieve pattern transfer from the BCP template into SiO_x , fluorine-based etch chemistries are routinely used for similar purposes.

For lift-off applications, the arguably ideal BCP template would be one adopting a self-assembled morphology with cylindrical minority domains oriented perpendicular to the substrate and which can selectively be eliminated to create an isoporous structure. Candidate commercially available BCP material systems include PS-*b*-PMMA and poly(styrene-*block*-lactic acid) (PS-*b*-PLA) as the PMMA and PLA blocks can selectively be removed in a ‘wet’ process utilizing

UV-induced chain scission[27] and alkaline hydrolysis (or enzyme-catalyzed degradation) [42], respectively. Implementing the nanoporous BCP template using SISR, which entails the geometrical redistribution of the constituent blocks of the minority domains rather than their elimination, would, however, be an attractive alternative considering the procedure’s comparative simplicity, reversibility, and potential for less harsh processing conditions. Furthermore, it might also enable the use of a wider range of BCPs for this type of nanopatterning.

As isoporous membranes for ultra-/nanofiltration applications [43, 44] and nanofabrication templates [9, 34, 35, 45, 46] have previously been fabricated using SISR of PS-*b*-P_xVP films, we here investigate if this approach reliably can be used in a large-area lift-off scheme. Hence, a thin (~21 nm) BCP template composed of a mixture of a linear diblock PS-*b*-P2VP and a lower molecular weight *homopolystyrene* (*h*PS) species is explored as a proof-of-concept. The BCP film is believed to spontaneously adopt a morphology consisting of a monolayer of hexagonally ordered, non-close-packed P2VP spheres in a PS matrix during SVA, however, as the film thickness approximately equals the diameter of the minority domains [and close to half the *center-to-center* (c-c) pitch] it is technically difficult to differentiate a spherical morphology from one of short cylinders oriented perpendicular to the substrate.

Consequently, we here opt for a three-layer lift-off stack consisting of, from the substrate up, a water-soluble PVA sacrificial layer, a SiO_x intermediate hardmask, and a PS-*b*-P2VP + *h*PS film for pattern generation. We demonstrate that highly ordered, large-area arrays of metal NPs can be implemented rapidly and cost-effectively using a method that combines the strengths of BCP self-assembly with those of a multi-layer lift-off stack. The developed process flow is schematically illustrated in figure 1.

2. Experimental

2.1. Materials

PS-*b*-P2VP ($M_n = 44.0\text{--}18.5\text{ kg}\cdot\text{mol}^{-1}$, *polydispersity index* (*PDI*) = 1.07) and *h*PS ($M_n = 12.5\text{ kg}\cdot\text{mol}^{-1}$, *PDI* = 1.04) were purchased from Polymer Source Inc., Canada. E-beam evaporated SiO_2 (99.99%, Kurt J. Lesker) were used for the intermediate hardmask while the sacrificial layer consisted of partially hydrolyzed PVA ($M_w \sim 31\text{ kg}\cdot\text{mol}^{-1}$, 86.7–88.7 mol% hydrolyzed, Mowiol 4-88, Sigma-Aldrich). HSQ (XR-1541, 2%, Dow Corning) and Dx ($M_n \sim 70\text{ kg}\cdot\text{mol}^{-1}$, Pan-Reac AppliChem) were evaluated as an alternative intermediate hardmask and sacrificial layer, respectively. Toluene (Selectipur, Merck) was the solvent for the PS-*b*-P2VP + *h*PS mixture and was also used during the SVA of the BCP layer. SISR was performed using ethanol ($\geq 99.8\%$, AnalaR NORMAPUR, VWR) or isopropanol (GPR Rectapur, VWR). The metals deposited were *titanium* (Ti) and *gold* (Au, 99.99%) and the substrates used were 100 mm Si(100) wafers.

2.2. Polymer solutions

The BCP solution was prepared by mixing *hPS*, *PS-*b*-P2VP*, and toluene at room temperature (*RT*, $\sim 21^\circ\text{C}$), heating the sealed vial to $\sim 60^\circ\text{C}$ and maintaining this temperature for 60 min during continuous stirring. The total polymer concentration was 0.90 % (w/w) with *hPS* constituting 30 % (w/w) of the total amount of polymer. The 4 % (w/w) PVA solution was prepared analogously to that of the BCP but now using deionized (DI) water, a temperature of $\sim 80^\circ\text{C}$ and elevated temperatures for 90–120 min. Both solutions were further left to stir overnight at *RT* before passing them through 0.1 μm PTFE syringe filters (Whatman) once.

2.3. Ashing

All instances of *ashing*, i.e. subjecting a sample to an oxygen plasma, in this study were used to either completely remove a polymer layer or as a surface treatment—not as a pattern transfer technique—and should thus not be confused with the later pure oxygen PVA RIE (RIE III, see figure 1). A TePla 300 Microwave Plasma System was used to this end. One high (1000 W, 50 sccm O_2) and one low (100 W, 50 sccm $\text{O}_2 + 50$ sccm N_2) RF power recipe, of variable duration, were used and hereon denoted ‘*high power*’ and ‘*low power*’, respectively.

2.4. Ascertaining RIE etch rates

In ascertaining the nominal time-average *ERs* and *ER* selectivities of our chosen stack materials in RIE I–III, a number of preliminary RIE runs were conducted. A largely rebuilt Advanced Vacuum Vision 320 RIE and sets of Si(100) sample pieces ($\sim 10 \times 10 \text{ mm}^2$), each clad with a single thick, unstructured layer of one of the relevant materials, were used in this endeavor. All samples were used only once and spectroscopic reflectometry (K-MAC ST4000-DLX, normal incidence, wavelength interval $\lambda = [400, 800] \text{ nm}$)—performed before and after each run—was used to measure the simultaneously induced changes in film thickness of the different materials as a consequence of the applied RIE procedure. The settings evaluated for RIE I–III were {550 W, 45 sccm $\text{CHF}_3 + 5$ sccm O_2 , 20 mTorr}, {400 W, 25 sccm $\text{CHF}_3 + 25$ sccm Ar, 15 mTorr} and {100 W, 50 sccm O_2 , 15 mTorr}, respectively.

2.5. Lift-off experiments

After ashing (*high power*, 2 min) the Si(100) wafer, the PVA layer was applied through spin-coating (6000 rpm) and then soft-baked (110°C , 4 min). Next, a layer of SiO_x was deposited via e-beam evaporation (*base pressure*, $BP = 2.3 \cdot 10^{-6} \text{ Torr}$, rate $\sim 1 \text{ Å} \cdot \text{s}^{-1}$) and ashed (*low power*, 2 min) prior to spin-coating (6000 rpm) the BCP film. Spectroscopic reflectometry was used to ascertain the film thicknesses along the way and the final sample stack was *PS-*b*-P2VP* + *hPS* ($\sim 21 \text{ nm}$)/ SiO_x (21 nm)/PVA (57 nm)/Si. The subsequent SVA procedure was performed at *RT* in a custom-built flow-based setup using toluene vapors (steady-state

$p_{\text{toluene}}/p_{\text{toluene}}^* = 0.97$ for 60 min). The parent wafer was then split into smaller pieces ($\sim 10 \times 10 \text{ mm}^2$) that for the purpose of SISR were immersed in isopropanol for 20 min and individually dried with a N_2 -gun. Next, the samples were subjected to RIE I–III, varying the durations of the second and third steps (table 2). Finally, 3.5 nm Ti and 10 nm Au was deposited via e-beam evaporation ($BP = 2.3 \cdot 10^{-6} \text{ Torr}$, rate $\sim 1 \text{ Å} \cdot \text{s}^{-1}$) before immersing the samples in 50°C DI water for ~ 2 min to enact the lift-off.

2.6. Sample characterization

Digital photography and scanning electron microscopy (SEM; Zeiss 1530, in-lens SEII detector, 5 kV acceleration voltage, $\sim 3 \text{ mm}$ working distance) were used to document the outcome of the lift-off experiments. The distributions of the top-view cross-sectional size, shape, and c-c interparticle distance of the Au NPs were characterized using digital image analysis (DIA) of SEM images acquired at 200k and 400k magnification. The DIA was performed using the software Cellprolifer 3.18 and in brief, the utilized pipeline is as follows: (i) subtraction of a background generated using a large Gaussian filter, (ii) application of a 5×5 pixel sweeping median filter for noise reduction, (iii) object identification using either the Otsu or the default settings of the minimum cross-entropy (MCE) thresholding method and (iv) extraction of relevant object descriptors. None of the NPs touching the image border were included in the characterization. An equivalent procedure was applied to nanopores except that an intensity inversion step was introduced in the pipeline prior to (i) and only Otsu was utilized. DIA was also performed on SEM images acquired at 50k magnification to map lattice vacancies by thresholding the image after (i), then dilating, eroding and inverting it prior to performing object identification and characterization.

To examine the side-view cross-sectional morphology, degree of crystallinity, and chemical composition of the NPs on select lift-off samples, scanning transmission electron microscopy (STEM) and energy-dispersive x-ray spectroscopy (EDS) were additionally performed at 200 kV in a probe-corrected FEI Titan Themis 200 equipped with a SuperX EDS detector. DIA of TEM images was performed in ImageJ v1.53 using Otsu thresholding. The TEM-lamellae were prepared following the *in situ* lift-out method in a Zeiss Crossbeam 550 (Ga^+ ion beam). To reduce ion beam-induced damages to the substrate and NPs, a carbon-rich capping layer was initially deposited using a C-pen. The final cleaning of the lamellae was implemented using a 5 kV (50 pA) ion acceleration voltage. The chemical composition maps were compiled using the python-based package *Hyperspy* (v1.6.2). To negate the influence of the Cu TEM grid, the EDS spectra were deconvoluted with the Cu signal.

Optical properties of the surface-supported Au NP arrays were also evaluated using spectroscopic ellipsometry (SE; Woollam RC2-XI, incidence angles $\{65^\circ, 70^\circ \text{ and } 75^\circ\}$, photon energy range, $E = [0.73, 5.9] \text{ eV}$). The relative permittivity $[\epsilon(E) = \epsilon_1(E) + i\epsilon_2(E)]$ and thickness (h_{eff}) of the effective media formed by the mixture of air and

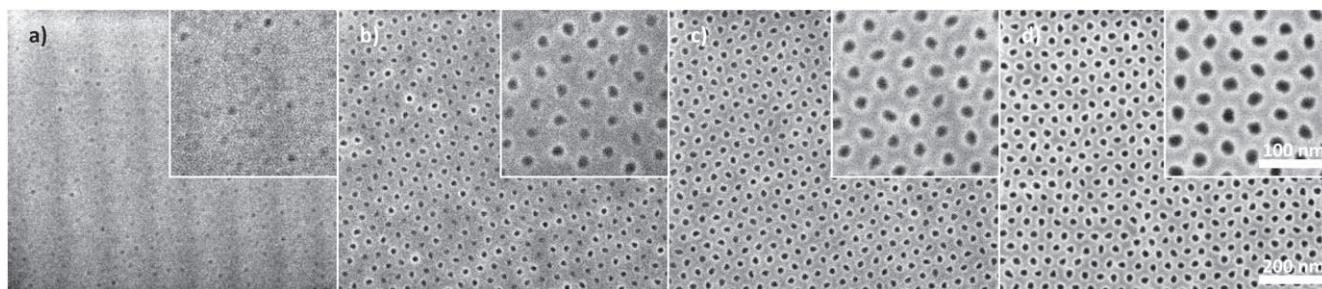


Figure 2. SEM-inspection of the HSQ layer in a stack originally consisting of PS-*b*-P2VP + *h*PS/HSQ/Si after sequentially performing a SISR, a generic SiO₂ etch of duration (a) 15 s, (b) 20 s, (c) 25 s and (d) 30 s, and finally an ashing (*high power*, 5 min).

supported NPs were modeled by fitting oscillator functions to the SE data using the software CompleteEase. A PSemi-Tri and two PSemi-M0 oscillators were used to account for the *localized surface plasmon resonance* (LSPR) and background, respectively. Using the SE-modelled ϵ and h_{eff} , absorbance spectra were calculated as well using a transfer matrix methodology.

3. Results and discussion

3.1. Process characterization of the RIE steps

Prior to attempting the intended lift-off scheme, the selected RIE I-III processes were evaluated with the explicit purpose of establishing the *ERs* of our chosen materials and to verify that sufficiently high *ER* reproducibility and selectivity between materials could be achieved. Note that for RIE II (SiO_x etch) and III (PVA etch), the *ERs* of the materials in unpatterned films were investigated here.

3.1.1. RIE I ('Descumming'). To demonstrate that the SISR-induced relief pattern in the BCP film indeed can be transferred to an underlying SiO_x layer, a standard SiO₂ RIE recipe, containing CHF₃ and O₂ and with a reported SiO₂ *ER* of $\sim 35 \text{ nm} \cdot \text{min}^{-1}$, was applied to a series of samples with a PS-*b*-P2VP + *h*PS/HSQ/Si stack. Although the sought proof of concept was obtained, a delayed onset in the patterning of the HSQ layer was observed and interpreted as the SISR not generating fully open pores (figure 2). The SISR consisted of sample immersion in ethanol, at *RT*, for 30 min followed by N₂-gun drying. As the applied RIE recipe contains oxygen, it is likely less suited to achieving a high *ER* selectivity between the SiO_x and the BCP template. Consequently, the BCP-to-SiO_x pattern transfer was divided into two sequential steps: (i) an initial 'descumming' step (RIE I) using the recipe above and with the explicit purpose of removing the residual polymer at the bottom of the BCP pores prior to (ii) a dedicated oxygen-free SiO_x etch (RIE II, see below). A 20 s RIE I, as used in figure 2(b), was adopted as our default descumming procedure as it seemingly opened all of the inspected pores.

3.1.2. RIE II (SiO_x etch). To maximize the $ER_{\text{SiO}_x} : ER_{\text{BCP}}$ and $ER_{\text{SiO}_x} : ER_{\text{PVA}}$ selectivities, a RIE II process containing CHF₃

and Ar was selected. Two sets of RIE II experiments were conducted to ascertain the *ERs* of, and selectivities between, the materials involved in our intended lift-off stack. In the first set, samples clad with a single layer of our BCP mixture, PVA, HSQ, and sputter-deposited SiO_x were studied. The RIE II process resulted in a marginal increase of the BCP film thickness, high *ERs* of both HSQ and SiO_x, and a modest PVA *ER* (see table 1 which is a summary of tables S1-S3). Substrate-selective deposition of fluoropolymers, due to plasma-induced polymerization of CHF₃, is thought to be the cause of the apparent increase in the BCP layer thickness.

As a high $ER_{\text{SiO}_x} : ER_{\text{PVA}}$ would mitigate propagation (and amplification) of any variation in depth between nanopores, potentially accrued during the SISR, RIE I, and/or RIE II in our intended lift-off scheme, a second set of RIE II experiments were conducted focusing on the sacrificial material beneath this interface. Dx was also included as an alternative to PVA and Dx was found to etch, on average, $\sim 54 \%$ faster than PVA leading to $ER_{\text{HSQ}} : ER_{\text{PVA}} = 4.0$ and $ER_{\text{HSQ}} : ER_{\text{Dx}} = 2.6$ while the corresponding selectivity values toward sputter-deposited SiO_x were slightly lower (table 1). We thus opted to proceed using PVA over Dx as our sacrificial layer material. We note, however, that the PVA *ER* is nearly twice as high in this set of RIE II experiments as in the first despite all *ERs* being highly consistent between runs within each set of experiments (table 1). As water-induced swelling of the PVA films during storage was eliminated, varying degrees of material deposition following CHF₃ polymerization is a conceivable explanation.

3.1.3. RIE III (PVA etch). As the SiO_x intermediate hardmask ought to be highly stable in an oxygen plasma, a pure oxygen RIE III process was selected. The PVA *ER* was evaluated at two RF power settings (100 and 200 W) of which the lower was ultimately selected for a slower, more controlled process (table 1).

3.2. Lift-off experiments

Samples with uniform PS-*b*-P2VP + *h*PS ($\sim 21 \text{ nm}$)/SiO_x (21 nm)/PVA (57 nm)/Si stacks were implemented as outlined in section 2.5. SEM verification of the sought BCP surface topography was obtained after the SVA and SISR steps (figure 3).

Table 1. Summary of the RIE II and III process characterization experiments.

RIE II—experiment 1 ($n = 5$) ^a			ER selectivities		
Material	$\langle ER \rangle^b$ [nm·min ⁻¹]	SD_{ER}^c [nm·min ⁻¹]	Materials	$\langle ER_1/ER_2 \rangle$	SD
BCP ^d	-1.6	0.9	HSQ:BCP	-42.7	32.1
HSQ ^e	44.5	1.0	HSQ:PVA	7.4	0.9
SiO _x ^{e,f}	32.7	1.2	SiO _x :PVA	5.5	0.7
PVA	6.1	0.7	PVA:BCP	-5.8	4.4
RIE II—experiment 2 ($n = 5$) ^a			ER selectivities		
Material	$\langle ER \rangle^b$ [nm·min ⁻¹]	SD_{ER}^c [nm·min ⁻¹]	Materials	$\langle ER_1/ER_2 \rangle$	SD
HSQ ^e	45.1	1	HSQ:PVA	4.0	0.1
SiO _x ^{e,f}	42.8	3.5	HSQ:Dx	2.6	0.1
PVA	11.4	0.4	SiO _x :PVA	3.8	0.3
Dx	17.6	0.7	SiO _x :Dx	2.4	0.1
RIE III—experiment 1 ($n = 7$) ^g					
Material	RIE power [W]	$\langle ER \rangle^b$ [nm·min ⁻¹]	SD_{ER}^c [nm·min ⁻¹]		
PVA	100	105.8	4.5		
"	200	204.3	10.1		

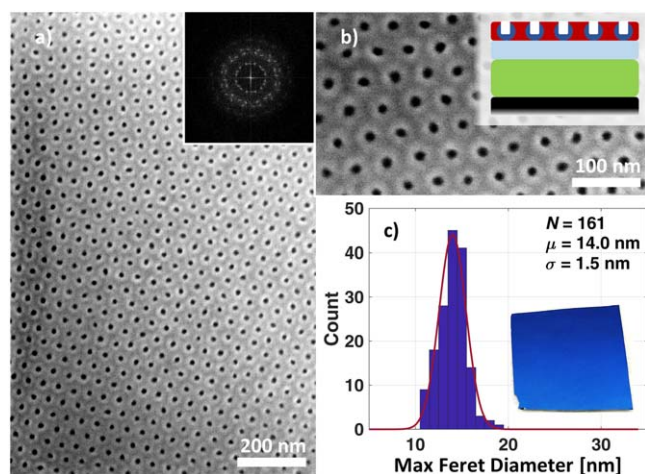
^a Number of replicates (i.e. RIE runs) in experiment.^b $\langle ER \rangle$ = time average etch rate.^c SD_{ER} = standard deviation of etch rate.^d 30% hPS + PS-*b*-P2VP.^e Ashed: *high power*, 1 min.^f Deposited using reactive sputter deposition.^g Number of runs for each RF power setting.

Figure 3. Structure verification, via SEM, after the solvent-induced surface reconstruction of the BCP template [(a) and (b)]. A histogram and fitted normal distribution of the DIA-measured polymer pore max Feret diameter is presented in (c). N , μ and σ are the number of measured pores and the mean and standard deviation of the fitted normal distribution, respectively. Inset are a 2D Fourier transform of the SEM image in (a), a schematic representation of the lift-off stack and a photo of a representative sample in (a), (b) and (c), respectively.

As confinement effects can reduce the effective ER at the bottom of high aspect ratio trenches and holes, optimal values for the RIE II and III durations (t_{II} and t_{III} , respectively) thus remain the most pertinent unknowns. This is further reinforced by the fact that the effects of these settings on the resultant nanopore sidewall profile are also uncertain. Stack

Table 2. Lift-off experiment—RIE DoE scheme.

RIE II ^a		RIE III ^b		Stack release
t_{II} [s]	EF_{SiOx}^c	t_{III} [s]	EF_{PVA}^c	
37	1.25	40	1.25	Full
"	"	43	1.35	"
"	"	46	1.45	"
44	1.50	40	1.25	"
"	"	43	1.35	"
"	"	46	1.45	"

^a $ER_{SiOx} = 42.8$ nm·min⁻¹.^b $ER_{PVA} = 106.5$ nm·min⁻¹.^c Etch factor, $EF \equiv (ER \cdot t)/h$.

release during lift-off is generally aided by having a template with nanopores exhibiting a high aspect ratio and a *negative sidewall profile* (i.e. having a larger diameter at the substrate than at the top surface). These attributes reduce the risk of metal deposits along the nanopore sidewalls to form continuous bridges that anchor the top layer and prevent its release or alternatively, rip NPs from the substrate. Sidewall deposits can further remain attached to the NP circumference, creating ear-like structures. Consequently, a small *design of experiment* (DoE) matrix covering sets of predetermined EF s (EF_{SiOx} and EF_{PVA} for RIE II and III, respectively) was formulated (table 2). EF is here defined as the ratio between the nominal etch depth that would be obtained on an unpatterned film and the measured thickness of the target stack layer i.e. $EF \equiv (ER \cdot t)/h$, where t and h are the *etch duration* and measured target *layer thickness*, respectively.

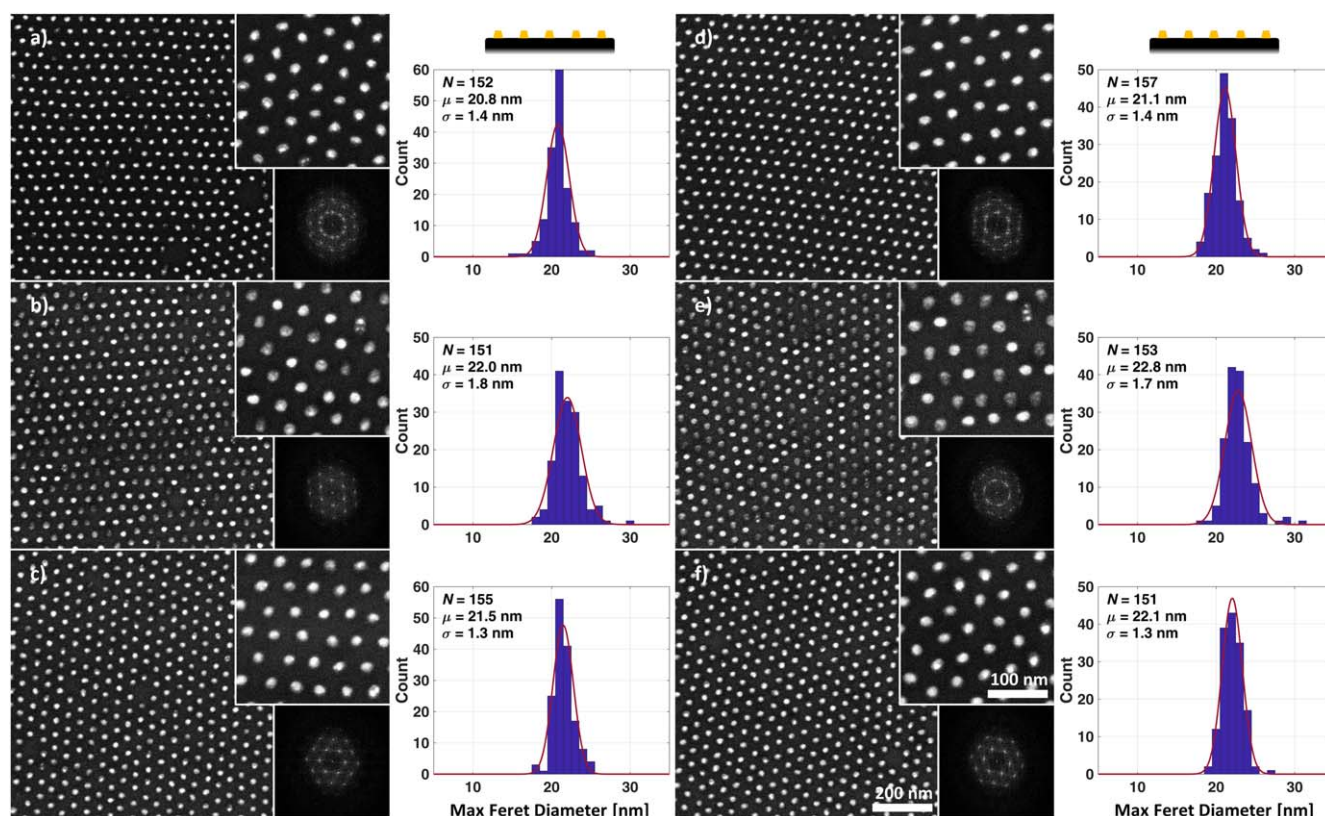


Figure 4. Compilation of SEM images, acquired after lift-off, of the Au NP arrays and histograms (with fitted normal distributions) of the DIA-measured max Feret diameters. Inset are also 2D Fourier transforms of SEM images acquired at the lower level of magnification displayed here. N , μ and σ are the number of measured NPs and the mean and standard deviation of the fitted normal distributions, respectively. EF_{SiO_x} was 1.25 [(a)–(c)] or 1.50 [(d)–(f)] while EF_{PVA} was 1.25 [(a) and (d)], 1.35 [(b) and (e)] or 1.45 [(c) and (f)].

The samples went from a deep blue prior to RIE I–III [figure 3(c)], to various shades of brown after the dry etching steps [figure S1(a)–(f) (available online at stacks.iop.org/NANO/33/325302/mmedia)]. After deposition of 3.5 nm Ti and 10 nm Au, lift-off was enacted through sample immersion in 50 °C DI water and complete stack release was achieved immediately on all samples [figure S1(g)–(l)].

SEM-inspection and accompanying DIA reveal highly ordered arrays of uniform, well-separated NPs throughout the RIE DoE scheme, as evidenced by the narrow NP size and shape distributions and the structured 2D Fourier transforms of the SEM images (figure 4, table S4). Here MCE and Otsu thresholding, during the SEM image DIA, was applied for NPs and pores, respectively, unless otherwise stated. The mean max Feret diameters and c-c interparticle distances are found to be in the ranges [21, 23] nm and [42, 44] nm, respectively. Although instances of lattice vacancies and less bright NPs can be observed, further DIA of images taken at 50k magnification suggest that the non-patterned area fraction is ≤ 3.0 % (figure S2 and table S5).

Cross-sectional structural and compositional analyses were also performed, on NPs from the $\{EF_{SiO_x} = 1.50, EF_{PVA} = 1.25\}$ sample, using STEM and EDS elemental mapping, respectively. Well separated Au NPs, embedded in a C-rich and O-containing capping layer, can be observed resting on Ti adhesion layers (figure 5). The height of the Au particles ([9, 10] nm) is in good

agreement with the nominal thickness of the deposited Au layer, however, both the measured diameter ([10, 14] nm) and the c-c pitch ([14, 16] nm) are smaller than those obtained previously by DIA of top-view SEM images (figure S3 and table S6). This can be explained by the orientation of the NP hexagonal lattice in relation to the viewing plane, the thickness of the TEM lamella and potentially also material loss during sample preparation.

A number of dark wavy striations were visually observed on the lift-off samples after RIE III which were not discernable prior to RIE I [figure S1(a)–(f)]. A darker shade here suggests that less material is removed from the stack during RIE I–III. Similar dark lines—likely of the same origin—were also seen in low magnification SEM images acquired after the lift-off step but now represent areas containing less metal (figure S4). The results of a follow-up experiment in which different SISR solvents, sample immersion times and drying techniques were evaluated suggest that the nature of these irregularities depend on the solvent removal kinetics at the end of the SISR step (figure S5). This can presumably cause variations in the resultant BCP nanopore depth such that a varying extent of descumming (RIE I) is required over the sample surface. Visually darker regions, after RIE III, would thus signify areas containing nanopores that have received an insufficient descumming. Potential ways to mitigate this issue are discussed below in section 3.4.

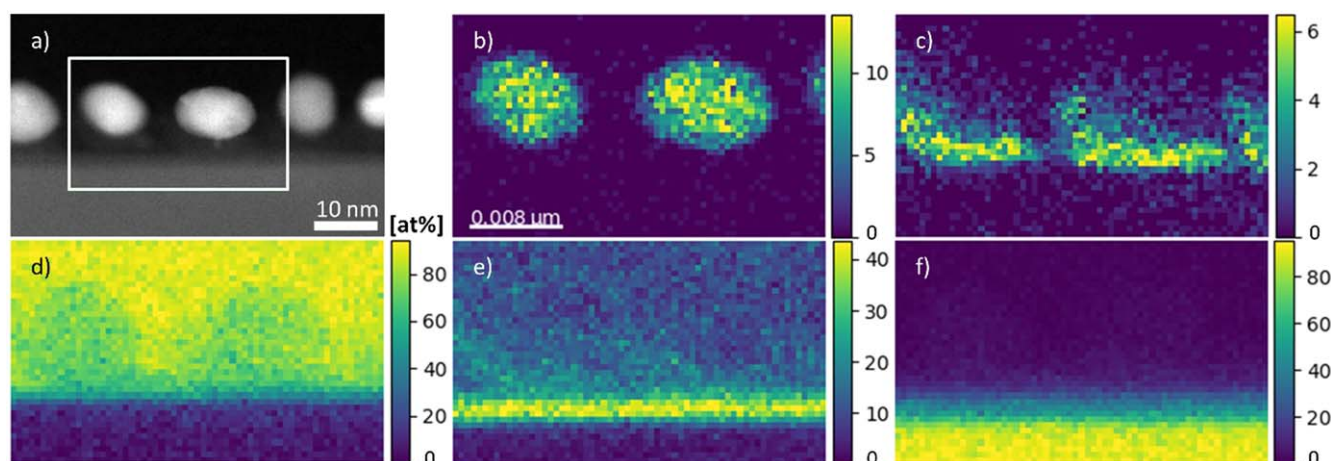


Figure 5. Dark-field STEM image (a) and EDS elemental maps [(b)–(f)] of a sample cross-section taken perpendicular to the substrate surface of the lift-off sample for which $\{EF_{\text{SiO}_2} = 1.50, EF_{\text{PVA}} = 1.25\}$ were used. The elements mapped are Au (b), Ti (c), C (d), O (e), and Si (f). The NPs are embedded in an organic polymer during lamella preparation, which causes pronounced C and O signals.

3.3. Optical properties of the Au NP arrays

The ability of NPs of free electron-like metals (e.g. Ag, Au and Al) to support LSPRs has found them applications within various scientific fields such as in light-trapping schemes in photovoltaic devices [1–4], surface-enhanced Raman spectroscopy [5], and photochemistry [47, 48]. SE was performed to optically characterize the LSPRs of the surface-supported Au NPs arrays with the mixed layer of air and NPs on the surface modelled as an effective homogeneous medium with *relative permittivity* ($\epsilon = \epsilon_1 + i\epsilon_2$) and *thickness* (h_{eff}). All samples exhibited similar optical properties with regards to the *position* ($E_{\text{LSPR}} \in [1.90, 2.35]$ eV), *amplitude* ($\epsilon_{2,\text{LSPR}} \in [0.20, 0.58]$) and *full width at half maximum* ($\in [0.40, 0.88]$ eV) of the peak in ϵ_2 associated with the LSPR [figures 6(a) and S6 and table S7]. The effective thickness, $h_{\text{eff}} \in [9.7, 14.2]$ nm is in good agreement with the height of the Au NPs, as previously determined by TEM (figure S3 and table S6), which is in line with prior results for similar structures [49]. A calculated NP layer absorptance of up to 19 % is observed if considering the effective medium layer when placed on an optical cavity [55 nm SiO_2 on a reflective Al film, see figure 6(c)]. The absorptance would increase further with slightly larger NPs and/or semiconductor coatings [4, 49].

3.4. Towards large-scale uniformity and reproducibility

3.4.1. SISR conducted at elevated temperatures. The geometry of the nanopores generated in the BCP film following a SISR procedure depends on the cavity bounded by the PS walls as well as the ultimate location and conformation of the P2VP blocks. Uniformity issues are thus readily explained if the ultimate location and conformation of the P2VP blocks depend on the solvent removal kinetics. As the amount of P2VP remains invariant, increasing the volume of the PS housing cavity might thus be one way of ensuring open shafts through their centers. This can be accomplished by performing the SISR at elevated

temperatures as, for a given SISR solvent and sample immersion time, the osmotic pressure inside the P2VP domains during sample immersion will increase with increasing solvent temperature. The higher osmotic pressure in combination with a simultaneous increase in PS block chain mobility [i.e. a lowering of the PS *glass transition temperature* (T_g)] due to solvent interaction, results in a plastic deformation of the PS matrix as the PS walls between P2VP domains are squeezed. The result is an increase in both the size of the PS cavities and the BCP film thickness while the minority domain c-c distance remains unchanged [44, 50–53]. This technique has previously been used on self-assembled PS-*b*-P2VP films containing perpendicularly oriented P2VP cylinders to generate fully open pores traversing the entire layer thickness [52, 53].

To investigate the applicability of this approach to the current lift-off scheme, SISR was performed using ethanol with temperatures ranging from $\sim 5^\circ\text{C}$ to $\sim 50^\circ\text{C}$ and a N_2 -gun to dry the samples afterward. SEM-inspection after RIE I–III does indeed reveal an increasing pore diameter with higher solvent temperature but, unfortunately, also that a large fraction of the inspected area remained unpatterned. Here, the clearly best results were obtained at *RT* (21°C), as determined by both SEM and the macroscopic appearance of the samples after RIE III (figure S7). Repeating the experiment using the simpler (PS-*b*-P2VP + *h*PS)/Si(100) stack and SEM-inspection directly after the SISR, provided further insight as to why unpatterned areas were observed in the previous experiment as it revealed that the BCP pattern becomes progressively more diffuse with increasing ethanol temperature (figure S8). The discrepancies between our results and those of Wei *et al* [52] and Yin *et al* [53] are conceivably accounted for by: (i) the lower degree of polymerization of our BCP species (PS_{44k}-*b*-P2VP_{18.5k} versus PS_{290k}-*b*-P2VP_{72k}), (ii) our inclusion of a high mass-fraction of a low molecular weight *h*PS species that ought to lower T_g of the PS matrix and/or (iii) differences in the initial BCP film morphology. The morphology of the referenced works employing this technique was one of perpendicularly oriented

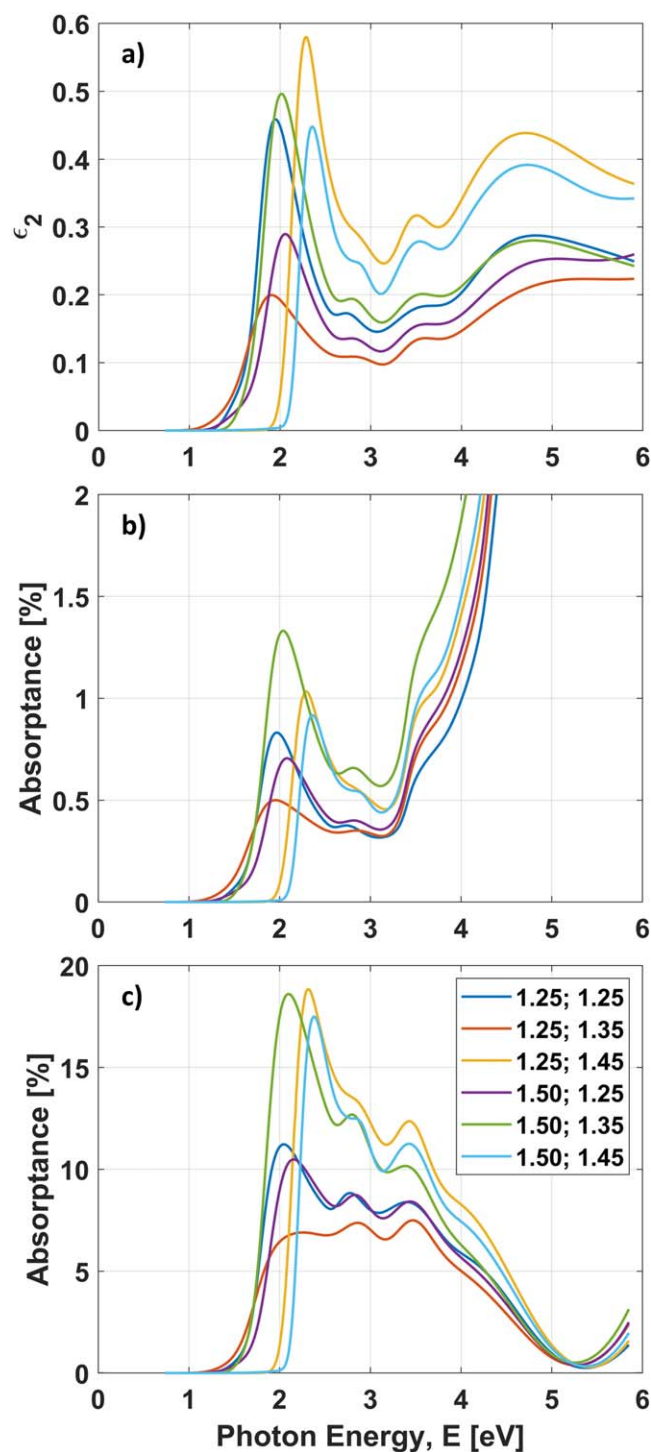


Figure 6. Plots of (a) the imaginary part of the relative permittivity (ϵ_2) and [(b) and (c)] calculated absorbance spectra of the effective media formed by the surface-supported Au NP arrays. In calculating the absorbance, the effective media were theoretically placed on an optically thick slab of Si in (b) whereas they rest on a 55 nm SiO_x layer on top of a reflective Al substrate in (c). The legend states the values of the sample-identifying EFs used during RIE II and III (i.e. $EF_{\text{SiO}_x}:EF_{\text{PVA}}$).

cylinders whereas in our case a monolayer of P2VP spheres is more likely considering (i) the substantial inclusion of *h*PS in the BCP film, (ii) the use of PS-selective toluene vapor in the SVA and (iii) observed terrace formation with the same

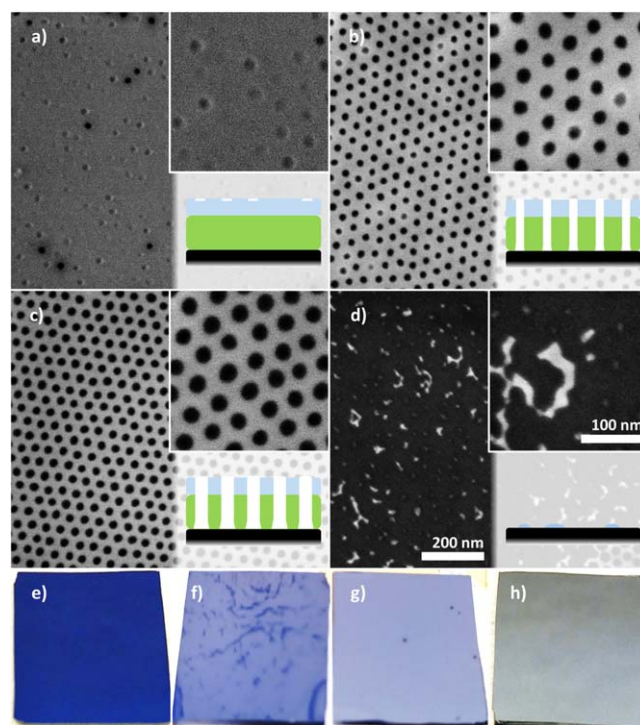


Figure 7. Compilation of SEM images [(a)–(d)] and photographs [(e)–(h)], acquired after RIE III, of samples subjected to a progressively longer duration of a mainly oxygen RIE I. The length of RIE I was 20 s [(a) and (e)], 30 s [(b) and (f)], 40 s [(c) and (g)], or 50 s [(d) and (h)].

top-view structure, believed to represent a double layer of spheres, when the BCP film thickness exceeds 21 nm by a couple of nanometers. Thus, while increased SISR temperature can be helpful to open cylindrical domains, this appears less effective for the current BCP system.

Although not investigated here, there are several other approaches that might eliminate or at least mitigate the macroscopic inhomogeneities. These include: (i) the use of dip-coating equipment in performing the SISR to achieve more uniform drying conditions, (ii) the prior selective sequestration of a species, able to e.g. H-bond to the P2VP blocks, within the P2VP domains for later extraction through solubilization [52, 54, 55] and (iii) the introduction of a cleavable moiety or block in-between the PS and P2VP blocks during the synthesis of the BCP [56–58]. Only minor adjustments of the here developed nanolithographic process flow would be required to apply any of these options.

3.4.2. Oxygen plasma descumming (Alt. RIE I). The reason for initially opting for a CHF_3 -containing descumming step was the ease by which the necessary duration could be gauged through inspection of the SiO_x layer beneath. A pure oxygen plasma RIE I process might, however, be more apt in alleviating the SISR-related uniformity issues as the SiO_x intermediate hardmask would then serve as an effective etch-stop and the duration of RIE I could be tailored to the shallowest pore post-SISR without affecting the SiO_x at the bottom of deeper pores. Consequently, propagation and amplification of initial variations in the degree of openness

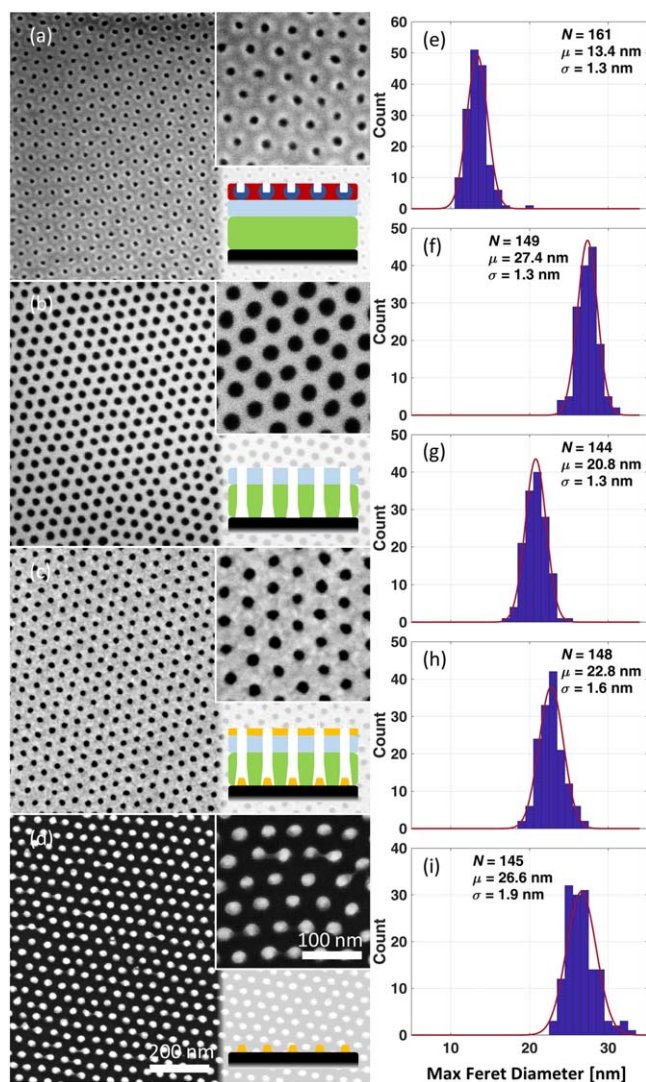


Figure 8. SEM images acquired after (a) SISR, (b) RIE I-III, (c) deposition of Ti and Au and (d) lift-off for the sample subjected to a 40 s oxygen-rich RIE I descumming. The histograms, and fitted normal distributions, in (e)–(g) refer to the max Feret diameters of the pore openings in (a)–(c) while those in (h) and (i) describe the resultant NPs in (d) when using the Otsu and MCE thresholding algorithm, respectively.

of the individual nanopores could be mitigated or even remedied. The drawback is the added erosion of the BCP template that will enlarge the pores and ultimately jeopardize its usefulness as an etch mask. To investigate this, new samples with a PS-*b*-P2VP + hPS (~ 21 nm)/SiO_x (21 nm)/PVA (82 nm)/Si lift-off stack were prepared using the same methodology as in the previous lift-off experiment except that ethanol, rather than isopropanol, was used in the SISR. RIE I-III were subsequently performed using an oxygen-rich RIE I descumming step {50 W, 45 sccm O₂ + 5 sccm Ar, 15 mTorr} of progressively increased duration in the sample series. The RIE II and III *EF*s were $EF_{SiO_x} = 1.50$ and $EF_{PVA} = 1.35$, respectively. SEM-inspection, after RIE III, reveals that a RIE I of > 30 s is required to open all the pores in the inspected areas [figures 7(a)–(c)]. After a 50 s RIE I only discrete remnants were, however, left of the intermediate

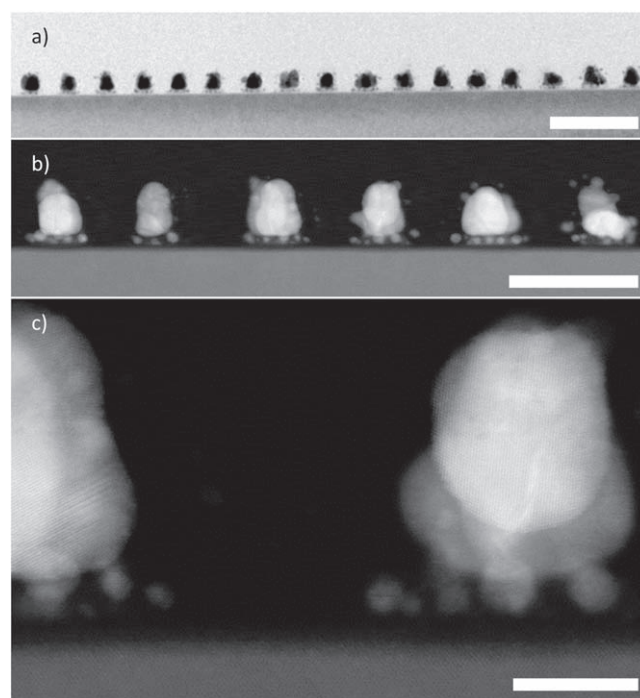


Figure 9. STEM images of sample cross-sections, from the sample in figure 8(d), acquired at different levels of magnification and in bright-field (a) or dark-field [(b) and (c)] mode. Note the atomic structure visible in (c). The scale bars are (a) 100 nm, (b) 50 nm, and (c) 10 nm.

hardmask, presumably due to the almost complete removal of the BCP template during the descumming step [figure 7(d)]. The visual appearance, after RIE III, of the samples subjected to a ≥ 30 s RIE I was dominated by light areas, suggesting mostly open pores after descumming. Further, the sample for which a 40 s RIE I was used was virtually uniform in appearance [figure 7(g)].

The sample depicted in figures 7(c) and (g) was proceeded to a full lift-off attempt, i.e. deposition of 3 nm Ti and 20 nm Au { $BP = 1.2 \cdot 10^{-6}$ Torr, $0.5 \text{ Å} \cdot \text{s}^{-1}$ } followed by immersion in 50 °C DI water. Subsequent SEM inspection and DIA reveals high-quality NPs with a larger average max Feret diameter (27 nm) than those in the first lift-off experiment (figure 8 and table S4) and a highly reduced number of lattice vacancies as only ~ 0.4 % of the area is unpatterned [figure S2(m)–(n) and table S5]. Cross-sectional STEM imaging and EDS elemental analysis were additionally performed on this sample and the imaging reveals slightly tapered NPs exhibiting a high degree of crystallinity (figure 9). Further, the NP diameter ([16, 25] nm) and c-c pitch ([37, 45] nm) are similar to those obtained from the top-view SEM images. Again, the height is also in good agreement with the amount of metal deposited (figure S9 and table S8). The main NPs are seen to be resting on a bed of smaller particles, suggesting that the nominally 3 nm of deposited Ti does not form a uniform adhesion layer (figures 9 and 10). Instances of additional smaller particles, as well as a diffuse corona of Ti, are also detected around the main NPs (figure 10). Conceivable explanations for these include

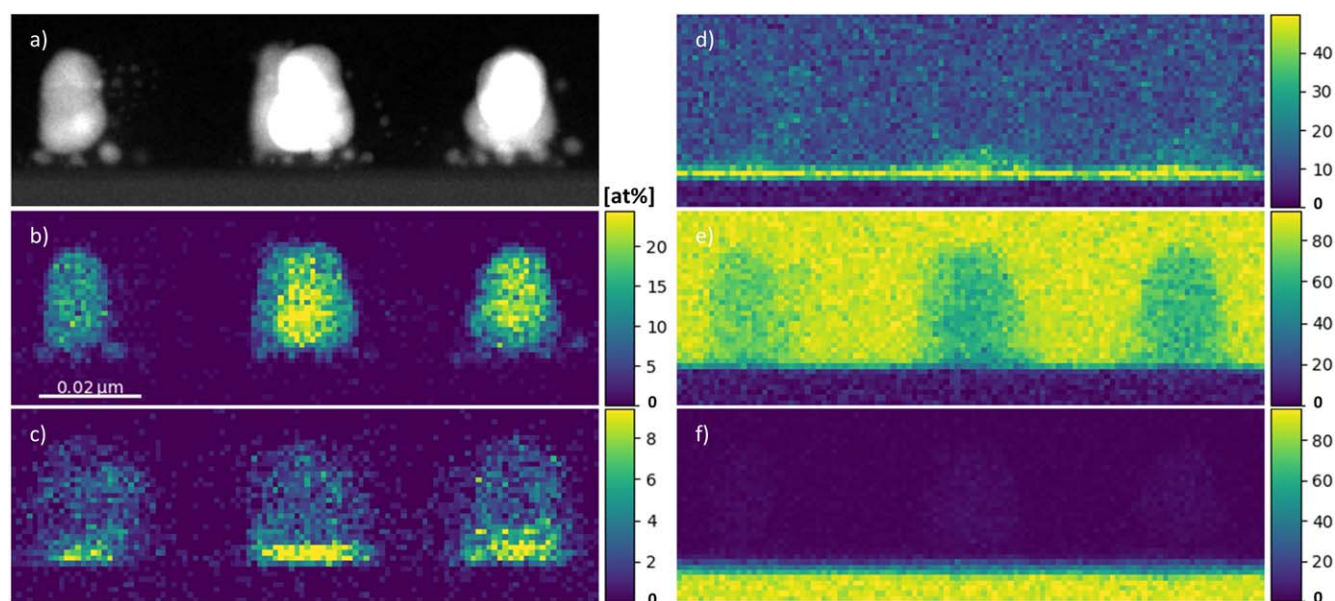


Figure 10. High-angle annular dark-field STEM image (a) and EDS Au (b), Ti (c), O (d), C (e), and Si (f) elemental maps acquired on cross-sections containing the high-quality NPs of the sample in figure 8(d).

material redistribution and redeposition during the preparation of the TEM lamellae or remnants from the top metal layer.

Although full stack release was not achieved on this sample—likely due to insufficient optimization of the RIE settings given the thicker PVA layer and the larger amount of Au deposited—it is believed that an oxygen-rich descumming can be useful for mitigating SISR-induced uniformity issues (figure S10).

4. Conclusions

A water-based lift-off scheme for generating arrays of surface-supported metal NPs using a (PS-*b*-P2VP + *h*PS)/SiO_x/PVA stack is demonstrated. The thin BCP film is believed to adopt a morphology consisting of a monolayer of hexagonally ordered, non-close-packed P2VP spheres in a PS matrix. SISR is successfully applied to the BCP film to generate a surface topography. A surface relief pattern, consisting of depressions in the P2VP domains, is thus obtained and subsequently transferred to the SiO_x and PVA layers beneath through a sequence of RIE steps. The result is a large-area, layered lithography mask containing an array of vertically oriented high aspect ratio nanopores, generated using a considerably thinner BCP template. After metal deposition, dense, highly ordered arrays of discrete metal NPs are ultimately obtained on the substrate by dissolving the sacrificial PVA layer in water. SE analysis shows that Au NP arrays fabricated with this protocol support the excitation of sharp LSPRs, indicative of high array uniformity and particle homogeneity.

The presented results may be considered a proof-of-concept for the generation of surface-supported NP arrays via a BCP-based lift-off scheme utilizing SISR and a water-soluble sacrificial layer. The developed nanofabrication

protocol ought to be compatible with a broad range of substrates and materials deposited by evaporation or other line-of-sight deposition methods, opening for many new applications of interest. Using other BCP film morphologies, generation of alternative feature patterns should also be possible with this approach. As the protocol involves the generation of highly ordered, high aspect ratio, nanoporous templates as an intermediate step, it could furthermore be of interest to various applications requiring such structures.

Acknowledgments

We acknowledge Olivier Donzel-Gargand for conducting the TEM-analysis and the Swedish Research Council (Reg. No. 621-2014-5599) and the Swedish Energy Agency (Project No. 45409-1) for financial support.

We acknowledge Myfab Uppsala for providing processing equipment and cleanroom facilities. Myfab is funded by the Swedish Research Council (2019-00207) as a national research infrastructure.

Data availability statement

The data that support the findings of this study are available upon reasonable request from the authors.

Notes

The authors declare no competing financial interest.

ORCID iDs

Carl Hägglund  <https://orcid.org/0000-0001-6589-3514>

References

- [1] Atwater H A and Polman A 2010 Plasmonics for improved photovoltaic devices *Nat. Mater.* **9** 205–13
- [2] Ferry V E, Munday J N and Atwater H A 2010 Design considerations for plasmonic photovoltaics *Adv. Mater.* **22** 4794–808
- [3] Hägglund C and Apell S P 2012 Plasmonic near-field absorbers for ultrathin solar cells *J. Phys. Chem. Lett.* **3** 1275–85
- [4] Hägglund C, Zeltzer G, Ruiz R, Wangperawong A, Roelofs K E and Bent S F 2016 Strong coupling of plasmon and nanocavity modes for dual-band, near-perfect absorbers and ultrathin photovoltaics *ACS Photonics* **3** 456–63
- [5] Willets K A and Van Duyne R P 2007 Localized surface plasmon resonance spectroscopy and sensing *Annu. Rev. Phys. Chem.* **58** 267–97
- [6] Corma A and Garcia H 2008 Supported gold nanoparticles as catalysts for organic reactions *Chem. Soc. Rev.* **37** 2096–126
- [7] Liu L C and Corma A 2018 Metal catalysts for heterogeneous catalysis: from single atoms to nanoclusters and nanoparticles *Chem. Rev.* **118** 4981–5079
- [8] Mistark P A, Park S, Yalcin S E, Lee D H, Yavuzcetin O, Tuominen M T, Russell T P and Achermann M 2009 Block-copolymer-based plasmonic nanostructures *ACS Nano* **3** 3987–92
- [9] Cho H, Park H, Russell T P and Park S 2010 Precise placements of metal nanoparticles from reversible block copolymer nanostructures *J. Mater. Chem.* **20** 5047–51
- [10] Lohmueller T, Bock E and Spatz J P 2008 Synthesis of quasi-hexagonal ordered arrays of metallic nanoparticles with tuneable particle size *Adv. Mater.* **20** 2297–302
- [11] Landeke-Wilmsmark B, Nyholm L and Hägglund C 2021 Process window for seeded growth of arrays of quasi-spherical substrate-supported Au nanoparticles *Langmuir* **37** 6032–41
- [12] Navlani-Garcia M, Salinas-Torres D, Mori K, Kuwahara Y and Yamashita H 2019 Tailoring the size and shape of colloidal noble metal nanocrystals as a valuable tool in catalysis *Catal. Surv. Asia* **23** 127–48
- [13] Keunen R, Macoretta D, Cathcart N and Kitaev V 2016 Stable ligand-free stellated polyhedral gold nanoparticles for sensitive plasmonic detection *Nanoscale* **8** 2575–83
- [14] Pangdam A, Wongravee K, Nootchanat S and Ekgasit S 2017 Urchin-like gold microstructures with tunable length of nanothorns *Mater. Des.* **130** 140–8
- [15] Xu D, Mao J, He Y and Yeung E S 2014 Size-tunable synthesis of high-quality gold nanorods under basic conditions by using H₂O₂ as the reducing agent *J. Mater. Chem. C* **2** 4989–96
- [16] Cha S K, Mun J H, Chang T, Kim S Y, Kim J Y, Jin H M, Lee J Y, Shin J, Kim K H and Kim S O 2015 Au–Ag core-shell nanoparticle array by block copolymer lithography for synergistic broadband plasmonic properties *ACS Nano* **9** 5536–43
- [17] Kruss S, Srot V, van Aken P A and Spatz J P 2012 Au–Ag hybrid nanoparticle patterns of tunable size and density on glass and polymeric supports *Langmuir* **28** 1562–8
- [18] Ross C A *et al* 2008 Si-containing block copolymers for self-assembled nanolithography *J. Vac. Sci. Technol. B* **26** 2489–94
- [19] Cheng J Y, Ross C A, Chan VZ-H, Thomas E L, Lammertink R G H and Vancso G J 2001 Formation of a cobalt magnetic dot array via block copolymer lithography *Adv. Mater.* **13** 1174–8
- [20] Hong A J, Liu C C, Wang Y, Kim J, Xiu F X, Ji S X, Zou J, Nealey P F and Wang K L 2010 Metal nanodot memory by self-assembled block copolymer lift-off *Nano Lett.* **10** 224–9
- [21] Shin D O, Jeong J-R, Han T H, Koo C M, Park H-J, Lim Y T and Kim S O 2010 A plasmonic biosensor array by block copolymer lithography *J. Mater. Chem.* **20** 7241–7
- [22] Brassat K, Kool D and Lindner J K N 2019 Modification of block copolymer lithography masks by O₂/Ar plasma treatment: insights from lift-off experiments, nanopore etching and free membranes *Nanotechnology* **30** 225302
- [23] Tu K-H, Bai W, Lontos G, Ntetsikas K, Avgeropoulos A and Ross C A 2015 Universal pattern transfer methods for metal nanostructures by block copolymer lithography *Nanotechnology* **26** 375301
- [24] Baruth A, Rodwogin M D, Shankar A, Erickson M J, Hillmyer M A and Leighton C 2011 Non-lift-off block copolymer lithography of 25 nm magnetic nanodot arrays *ACS Appl. Mater. Interfaces* **3** 3472–81
- [25] Chang C-C, Botez D, Wan L, Nealey P F, Ruder S and Kuech T F 2013 Fabrication of large-area, high-density Ni nanopillar arrays on GaAs substrates using diblock copolymer lithography and electrodeposition *J. Vac. Sci. Technol. B* **31** 031801
- [26] Kastle G *et al* 2003 Micellar nanoreactors—preparation and characterization of hexagonally ordered arrays of metallic nanodots *Adv. Funct. Mater.* **13** 853–61
- [27] Ferrarese Lupi F, Giammaria T J, Volpe F G, Lotto F, Seguíni G, Pivac B, Laus M and Perego M 2014 High aspect ratio PS-b-PMMA block copolymer masks for lithographic applications *ACS Appl. Mater. Interfaces* **6** 21389–96
- [28] Yang E L, Liu C C, Yang C Y P, Steinhaus C A, Nealey P F and Skinner J L 2010 Nanofabrication of surface-enhanced raman scattering device by an integrated block-copolymer and nanoimprint lithography method *J. Vac. Sci. Technol. B* **28** C6M93–6M97
- [29] Choi J W, Kim M, Safron N S, Arnold M S and Gopalan P 2014 Transfer of pre-assembled block copolymer thin film to nanopattern unconventional substrates *ACS Appl. Mater. Interfaces* **6** 9442–8
- [30] Lee D H, Shin D O, Lee W J and Kim S O 2008 Hierarchically organized carbon nanotube arrays from self-assembled block copolymer nanotemplates *Adv. Mater.* **20** 2480–5
- [31] Shin K, Leach K A, Goldbach J T, Kim D H, Jho J Y, Tuominen M, Hawker C J and Russell T P 2002 A simple route to metal nanodots and nanoporous metal films *Nano Lett.* **2** 933–6
- [32] Xiao S, Yang X, Edwards E W, La Y-H and Nealey P F 2005 Graphoepitaxy of cylinder-forming block copolymers for use as templates to pattern magnetic metal dot arrays *Nanotechnology* **16** S324–9
- [33] Jin C, Olsen B C, Luber E J and Buriak J M 2017 Nanopatterning via solvent vapor annealing of block copolymer thin films *Chem. Mater.* **29** 176–88
- [34] Park S, Wang J-Y, Kim B, Xu J and Russell T P 2008 A simple route to highly oriented and ordered nanoporous block copolymer templates *ACS Nano* **2** 766–72
- [35] Yoo H and Park S 2010 The fabrication of highly ordered block copolymer micellar arrays: control of the separation distances of silicon oxide dots *Nanotechnology* **21** 245304
- [36] Linder V, Gates B D, Ryan D, Parviz B A and Whitesides G M 2005 Water-soluble sacrificial layers for surface micromachining *Small* **1** 730–6
- [37] Marten F L 2002 Vinyl alcohol polymers *Encyclopedia of Polymer Science and Technology* (<https://doi.org/10.1002/0471440264.pst384>)

- [38] Eckelt A, Eckelt J and Wolf B 2011 Solubility of polymers *Encyclopedia of Polymer Science and Technology* (<https://doi.org/10.1002/0471440264.pst345>)
- [39] Lopes J F A and Simoneau C 2014 Solubility of polyvinyl alcohol in ethanol *EFSA Supporting Publ.* **11** 660E
- [40] Nam T *et al* 2019 Low-temperature, high-growth-rate ALD of SiO₂ using aminodisilane precursor *Appl. Surf. Sci.* **485** 381–90
- [41] Bennett B R, Lorenzo J P and Vaccaro K 1987 Low-temperature chemical vapor deposition of SiO₂ at 2–10 Torr *Appl. Phys. Lett.* **50** 197–9
- [42] Cummins C, Mokarian-Tabari P, Holmes J D and Morris M A 2014 Selective etching of polylactic acid in poly(styrene)-block-poly(d,l)lactide diblock copolymer for nanoscale patterning *J. Appl. Polym. Sci.* **131** 40798
- [43] Sun W, Wang Z G, Yao X P, Guo L M, Chen X Q and Wang Y 2014 Surface-active isoporous membranes nondestructively derived from perpendicularly aligned block copolymers for size-selective separation *J. Membr. Sci.* **466** 229–37
- [44] Ahn H, Park S, Kim S-W, Yoo P J, Ryu D Y and Russell T P 2014 nanoporous block copolymer membranes for ultrafiltration: a simple approach to size tunability *ACS Nano* **8** 11745–52
- [45] Park S, Yavuzcetin O, Kim B, Tuominen M T and Russell T P 2009 A simple top-down/bottom-up approach to sectorized, ordered arrays of nanoscopic elements using block copolymers *Small* **5** 1064–9
- [46] Gu X, Dorsey P and Russell T P 2012 High density and large area arrays of silicon oxide pillars with tunable domain size for mask etch applications *Adv. Mater.* **24** 5505–11
- [47] Meng X G, Liu L Q, Ouyang S X, Xu H, Wang D F, Zhao N Q and Ye J H 2016 Nanometals for solar-to-chemical energy conversion: from semiconductor-based photocatalysis to plasmon-mediated photocatalysis and photo-thermocatalysis *Adv. Mater.* **28** 6781–803
- [48] Naldoni A, Riboni F, Guler U, Boltasseva A, Shalae V M and Kildishev A V 2016 Solar-powered plasmon-enhanced heterogeneous catalysis *Nanophotonics* **5** 112–33
- [49] Hägglund C, Zeltzer G, Ruiz R, Thomann I, Lee H B R, Brongersma M L and Bent S F 2013 Self-assembly based plasmonic arrays tuned by atomic layer deposition for extreme visible light absorption *Nano Lett.* **13** 3352–7
- [50] Wang Y and Li F B 2011 An emerging pore-making strategy: confined swelling-induced pore generation in block copolymer materials *Adv. Mater.* **23** 2134–48
- [51] Wang Y 2016 Nondestructive creation of ordered nanopores by selective swelling of block copolymers: toward homoporous membranes *Accounts Chem. Res.* **49** 1401–8
- [52] Wei M J, Sun W, Shi X S, Wang Z G and Wang Y 2016 Homoporous membranes with tailored pores by soaking block copolymer/homopolymer blends in selective solvents: dissolution versus swelling *Macromolecules* **49** 215–23
- [53] Yin J, Yao X P, Liou J Y, Sun W, Sun Y S and Wang Y 2013 Membranes with highly ordered straight nanopores by selective swelling of fast perpendicularly aligned block copolymers *ACS Nano* **7** 9961–74
- [54] Jeong U, Ryu D Y, Kim J K, Kim D H, Wu X and Russell T P 2003 Precise control of nanopore size in thin film using mixtures of asymmetric block copolymer and homopolymer *Macromolecules* **36** 10126–9
- [55] Clodt J I, Rangou S, Schröder A, Buhr K, Hahn J, Jung A, Filiz V and Abetz V 2013 Carbohydrates as additives for the formation of isoporous PS-b-P4VP diblock copolymer membranes *Macromol. Rapid Commun.* **34** 190–4
- [56] Zhang M, Yang L, Yurt S, Misner M J, Chen J-T, Coughlin E B, Venkataraman D and Russell T P 2007 Highly ordered nanoporous thin films from cleavable polystyrene-block-poly(ethylene oxide) *Adv. Mater.* **19** 1571–6
- [57] Bang J, Kim S H, Drockenmüller E, Misner M J, Russell T P and Hawker C J 2006 Defect-free nanoporous thin films from abc triblock copolymers *J. Am. Chem. Soc.* **128** 7622–9
- [58] Gu W, Zhao H, Wei Q, Coughlin E B, Theato P and Russell T P 2013 Line patterns from cylinder-forming photocleavable block copolymers *Adv. Mater.* **25** 4690–5